sensors

MDPI

Article

How Geometry Affects Sensitivity of a Differential Transformer for Contactless Characterization of Liquids

Marc Berger *, Anne Zygmanowski and Stefan Zimmermann

Department of Sensors and Measurement Technology, Institute of Electrical Engineering and Measurement Technology, Leibniz University Hannover, 30167 Hannover, Germany; zygmanowski@geml.uni-hannover.de (A.Z.); zimmermann@geml.uni-hannover.de (S.Z.)
* Correspondence: berger@geml.uni-hannover.de; Tel.: +49-511-762-14648

Abstract: The electrical and dielectric properties of liquids can be used for sensing. Specific applications, e.g., the continuous in-line monitoring of blood conductivity as a measure of the sodium concentration during dialysis treatment, require contactless measuring methods to avoid any contamination of the medium. The differential transformer is one promising approach for such applications, since its principle is based on a contactless, magnetically induced conductivity measurement. The objective of this work is to investigate the impact of the geometric parameters of the sample or medium under test on the sensitivity and the noise of the differential transformer to derive design rules for an optimized setup. By fundamental investigations, an equation for the field penetration depth of a differential transformer is derived. Furthermore, it is found that increasing height and radius of the medium is accompanied by an enhancement in sensitivity and precision.

Keywords: differential transformer; contactless measurement; filed penetration depth; magnetic coupling; PCB coil; magnetic induced conductivity measurement

Citation: Berger, M.; Zygmanowski, A.; Zimmermann, S. How Geometry Affects Sensitivity of a Differential Transformer for Contactless Characterization of Liquids. *Sensors* **2021**, *21*, 2365. https://doi.org/10.3390/s21072365

Academic Editor: Edward Sabolsky

Received: 26 February 2021
Accepted: 26 March 2021
Published: 29 March 2021

1. Introduction

In certain applications, it is of great importance to determine the electrical and dielectric properties of a sample contactless in order to avoid sample contamination by the sensing system. Examples of these applications are the contactless blood conductivity measurement in medical technology as a measure of the sodium concentration or the contactless determination of the polarizability of a medium as a measure of the biomass in biotechnology. Since the sample or medium is often in materials with low permittivity such as polymers or glasses in these applications, contactless capacitive sensors usually suffer from poor penetration of the electric field through these materials. Thus, the sample is only exposed to a small amount of electric field, resulting in a lower sensitivity. For example, in [1], an investigation was made to determine the biomass through a polymer foil of a single-use bioreactor by a coplanar stripe line. Since most of the electric field was concentrated in the foil, these results were not promising. However, there are systems like capacitively coupled contactless conductivity detection (C^4D) [2], allowing for capacitive measure through a usually special fused-silica capillary with a small cross-section [3,4]. Nevertheless, due to the small cross-section of the capillary, C^4D is not suitable for in-line measurements where higher fluxes of the medium is expected. In addition, due to the above-mentioned poor penetration properties of the electric field through the capillary, the capillary wall can have a dominant influence on the impedance in this principle depending on the conductivity of the sample solution [5].

Inductive conductivity measuring systems can penetrate the materials much better, causing the sample to be exposed to a relatively high magnetic field strength. A typical configuration of inductive conductivity sensors consists of two coils immersed in and coupled by the liquid under test [6]. Due to the immersion of this sensor, it is not a contactless determination and is therefore not suitable for applications requiring the prevention of

sample contamination. Single-coil configurations can be used for contactless measurement. Here, the coil is placed close to the sample and the coil inductance is used as the measure, changing with varying electrical and dielectric properties of the sample [7]. However, the measurement signal is dominated by the primary field, resulting in an output voltage with a strong offset. Small changes in the secondary field B_S due to weak induced currents inside the medium are thus challenging to detect [1].

In this work, we use a differential setup consisting of three coils, giving a differential transformer. Differential transformers are already used in various sensing applications. One prominent example is the linear variable differential transformer, usually consisting of a movable magnetic soft iron or ferrite core inside a configuration of three coaxial coils [8–11]. These coils are arranged symmetrically to each other. The middle coil is the primary coil, excited by an alternating voltage of constant amplitude. The two outer coils are the secondary coils, which are connected differentially to each other. Due to this arrangement, a relative displacement of the ferrite core to the coils results in a disturbance of the symmetry, inducing a measurable output voltage at the differentially connected secondary coils. The output voltage corresponds very well with the displacement of the ferrite core, giving a high resolution and low noise displacement, position, or force sensors [12]. This type of application is well known and often used in practice [13–17].

In another setup, the ferrite core is fixed. If now a sample or medium is placed closer to one of the two secondary coils of the differential transformer, the asymmetry allows for measuring the electrical properties, such as the conductivity κ, and the dielectric properties, such as the polarizability ε', of the medium. Figure 1 schematically shows such a differential transformer and the equivalent electric circuit of the connected coils of an unloaded differential transformer. The measurement effect is based on eddy and displacement currents I_M within the medium, induced by the alternating primary field B_P. B_P is generated by the primary coil L_P, excited with U_P. These induced currents generate a secondary field B_S, counter-directed to the primary magnetic field. Due to the asymmetrical arrangement of the medium to the differential transformer, the secondary field better couples with the secondary coil L_{S1} closer to the sample than with L_{S2} and therefore induces a larger voltage into L_{S1}. As a result, an output voltage U_S can be measured at the output of the differentially connected secondary coils. Because of the differential setup of L_{S1} and L_{S2} and the symmetrical design of the two secondary coils relative to the primary coil L_P, the primary magnetic field does not induce a measurable voltage at the output of the connected secondary coils. This is a great advantage compared to configurations where only one single coil is used as described above; enabling even very low eddy and displacement currents I_M inside the medium to be detected. As pointed out earlier, magnetic fields can easily penetrate plastics and glass. Therefore, this measuring method is well suited for the contactless determination of the electrical and dielectric properties of liquids located inside a plastic or glass measuring (flow-through) chamber. Therefore, this measurement method has potential in biotechnology and medical technology for the contactless determination of biomass within single-use bioreactors [1,18] or for obtaining tissue information [19–23]. In addition, the differential transformer approach is investigated with respect to continuous in-line monitoring of the sodium concentration in human blood, by measuring the blood plasma conductivity, mainly influenced by the sodium concentration [24–27]. Continuous monitoring of plasma sodium concentration is particularly important in continuous renal replacement therapy, especially in patients with severe dysnatremia, since both a large deviation from the physiological plasma sodium level [26,28–30] and a rapid change in the concentration can lead to dangerous complications such as central pontine myelinolysis [31,32]. Continuous monitoring of this parameter enables the clinician to intervene as early as possible by individualized dialysis therapy [33–35]. The differential transformer is well suited for this application because it is based on a contactless measurement principle and thus avoids any risk of blood contamination during in-line measurement. In preclinical studies with reconfigured human blood in a dialysis system, we could already show in cooperation with the University Medical Center Göttingen, that

the differential transformer can be used to monitor the sodium concentration over a long period of time [36,37].

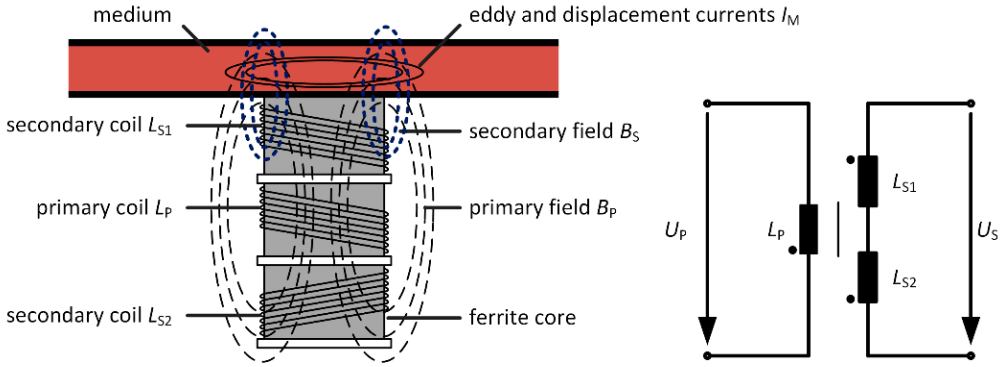

Figure 1. Depiction of the differential transformer consisting of three fixed coils on a ferrite core for the analysis of the electrical and dielectric properties of a medium in a measuring chamber or tubing (loaded) and its electrical equivalent circuit of the unloaded transformer. The secondary coils L_{S1} and L_{S2} are connected differentially in series.

In [1] it was demonstrated that the output voltage U_S of the differential transformer can be divided into a real part, depending on the polarizability ε' of the medium, and an imaginary part indicated by the imaginary unit j, depending on the conductivity κ and the dielectric losses ε'' as shown in Equation (1). This division of the output voltage is another advantage offered by the differential three-coil configuration.

$$U_S = U_P\left(-\omega^2 K\varepsilon' + j\,\omega K(\kappa - \omega\varepsilon'')\right) \tag{1}$$

ω is the angular frequency. U_P is the supplied input voltage of the primary coil L_P. K describes the magnetic coupling between L_P and the medium as well as the medium and the secondary coils L_{S1} and L_{S2}. Solutions to describe the magnetic coupling between wires and coils can be found, i.e., in [38]. In [39], an exact solution of the mutual inductance of two coils is given. However, for the case of the differential transformer, we have presented a mathematical model describing the coupling of the coils involving the medium in [37]. This mathematical model will be discussed in more detail in Section 3.1.2.

Due to the growing number of possible applications of a differential transformer for the characterization of liquids and thus increasing interest for this sensing concept, it is further investigated here. The objective of this work is to determine the basic effect of the sample geometry, such as the radius r_M of the medium and the height h_M of the medium, on the output signal of the differential transformer. Besides gaining a basic understanding, e.g., the effective sample volume, this knowledge shall additionally support the optimization of the design of new measurement chambers to achieve a maximum sensitivity of the differential transformer and thus improve the *SNR*.

2. Materials and Methods

2.1. PCB-Differential Transformer

For the experimental characterization, we use a differential transformer consisting of three planar printed circuit boards (PCB) containing conductive tracks of a height of 35 µm forming coils on a ferrite core. A photography of the used differential transformer is shown in Figure 2. All geometric dimensions are illustrated in Figure 3.

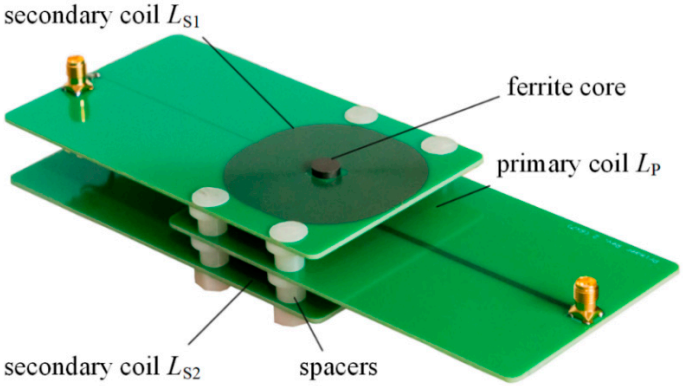

Figure 2. Photograph of the used differential transformer made of three printed circuit board (PCB) coils. The differential connection of L_{S1} and L_{S2} is realized via two wires (not seen).

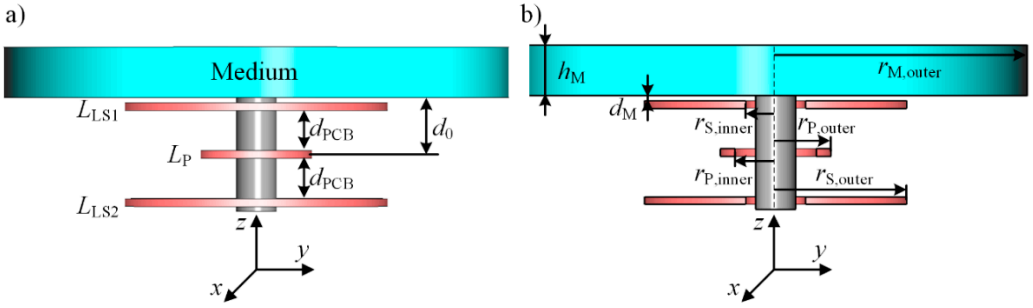

Figure 3. (**a**) Illustration of the CST-EM Studio simulation model. The number of windings of the primary coil excited with 1 V_{PP} is 42. The secondary coils L_{S1} and L_{S2} have 542 windings, and the direction of the winding of L_{S1} is opposite to L_{S2}. The distance d_{PCB} between the coils is 8 mm and the height of each PCB coil is 1.5 mm. d_0 is the distance between the medium and the primary coil. The coordinate system is defined as having the z-axis longitudinal to the ferrite core and the x- and y-axes in the radial direction. (**b**) Cross-section of the differential transformer with the height h_M and the outer radius $r_{M,outer}$ of the medium or the sample, respectively. $r_{P,inner}$ and $r_{P,outer}$ are the inner and outer radii of the primary coil L_P. Accordingly, $r_{S,inner}$ and $r_{S,outer}$ are the inner and outer radii of the secondary coils L_{S1} and L_{S2}.

The planar PCB coils enable the distance d_{PCB} between the primary coil L_P and the secondary coil L_{S1} as well as between the primary coil L_P and the secondary coil L_{S2} to be set precisely. By positioning these planar PCB coils at a defined distance from each other, the magnetic coupling between the coils and the medium can be affected. This can have positive effects on the sensitivity, as already discussed in [37]. Here, d_{PCB} is set to 8 mm via spacers. In addition, when the medium is positioned above L_{S1}, the flat design of these planar PCB coils enables all windings of the secondary coil L_{S1} to be close to the medium and hence L_{S1} is penetrated strongly by secondary field B_S. This results in a higher sensitivity of the differential transformer. All PCB coils were realized on a six-layer board, having the dimensions 90 × 120 × 1.5 mm. The ferrite core has a radius of 4 mm and a relative permeability μ_r of 300. The length of the ferrite core is 22 mm, penetrating all three PCB coils, as the total height of the three stacked coils is 20.5 mm. The upper and lower coils are the secondary coils L_{S1} and L_{S2} with a total number of windings n_S of 542 each, 91 windings on the top and bottom layer and 90 windings on the four middle layers. The track width of L_{S1} and L_{S2} is 0.1 mm with a clearance of 0.125 mm as well as an inner coil radius $r_{S,inner}$ of 6 mm resulting in an outer coil radius $r_{S,outer}$ of 26 mm. The inductivities L_{S1} and L_{S2} are each 23.8 mH with a DC resistance of 320 Ω. L_{S1} and L_{S2} are connected in series differentially via two wires. The middle coil is the primary coil L_P with a total of n_P = 42 windings, giving seven windings per layer. The track width is 0.3 mm with a clearance of 0.125 mm. The outer coil radius $r_{P,outer}$ is 11 mm and the inner coil radius $r_{P,inner}$ is 8.1 mm. However, the geometrical dimensions of the primary and secondary

coils will be discussed in detail later in this work. The inductance of L_P is 31.9 µH with a DC resistance of 3.4 Ω. The primary coil and the upper secondary coil L_{S1} have SMA connectors for the electrical connection. As can be seen from Equation (1), the output voltage U_S, and thus the sensitivity of the differential transformer, depends linearly on the voltage U_P applied to the primary coil L_P. In the investigations presented here, we excite L_P with 1 V_{PP} peak to peak, meaning the following sensitivity data always refer to this supply voltage. The choice of 1 V_{PP} has the advantage of enabling the sensitivities for other voltage U_P to be calculated easily and quickly, and making the obtained sensitivities comparable with previous publications [36,37]. In addition, Equation (1) reveals a dependency of the output voltage U_S and thus the sensitivity to the angular frequency ω or frequency f, respectively. It can be seen that a high frequency is generally desirable, as this increases the sensitivity. However, due to the always present stray capacitance between the windings of the coil, the frequency cannot be increased arbitrarily. These stray capacitances cause a resonant frequency. Above this resonance frequency, the coil has no inductive behavior. Therefore, f must always be lower than the resonance frequency. In [40], a possibility is described to estimate these stray capacitances and thus the resonance frequency a priori. Since we have coils with a rectangular cross section of the conductor and each coil has six layers, but in [40] only coils with isolated round conductors and at most three layers are considered, we have determined the resonant frequency experimentally. For the secondary coils, this is 250 kHz. Thus, at f = 155 kHz, the secondary coils behave as inductances. In all experiments, the sample is placed in different compartments defining the sample geometry on top of L_{S1}.

2.2. Test Solution

Deionized water (DI water) with different concentrations of sodium chloride (NaCl) is used for the experimental characterization of the differential transformer. The concentration is varied between 100 mmol/L and 150 mmol/L, as this range covers the clinically relevant pathological concentration range of sodium in blood serum, which is relevant for the above-mentioned monitoring during continuous renal replacement therapy [26,29,31–34]. Although the concentration generally has a non-linear impact on the sample conductivity [41], it could be shown in [36] that the imaginary part of the output voltage U_S of the differential transformer depends linearly on the concentration within this narrow range. The sensitivity S_c is determined by using the imaginary part of the output voltage $Im\{U_S\}$ at two different concentrations (e.g., c_1 = 100 mmol/L and c_2 = 150 mmol/L) according to Equation (2).

$$S_c = \frac{dIm\{U_S(c)\}}{dc} = \frac{Im\{U_S(c_2) - U_S(c_1)\}}{c_2 - c_1} \quad (2)$$

2.3. Simulation Model

In addition to the experimental tests, the setup is simulated using the CST-EM Studio. The basic simulation model is shown in Figure 3a, representing the differential transformer described above. d_0 is the distance between the primary coil L_P and the bottom of the medium and is 11.25 mm.

The coils are created in CST-EM Studio from a rectangular cross-section rotated around the z-axis. Using the coil generation tool, a number of windings, a wire resistance as well as a winding direction can be assigned to this coil. However, further geometrical factors, such as the conductor cross-section and filling factor, are not taken into account, whereby the winding-to-winding stray capacitances are also neglected. Therefore, it should be noted that this model is only valid at frequencies below the resonant frequency mentioned above and the measurements can only be compared with the simulations in this case. The direction of winding of L_{S1} is inverted to the direction of winding of L_{S2}. Thus, the sum of the induced voltages into L_{S1} and L_{S2} gives the output voltage U_S of the differential transformer. The voltage induced into each secondary coil can be derived from CST-EM Studios and divided into real and imaginary part. In contrast to the experimental tests,

the conductivity κ of the medium can be changed directly in the simulation model. The primary coil L_P is excited with 1 V_{pp} at a frequency of 155 kHz. The secondary coils L_{S1} and L_{S2} are excited with a current of 0 A, corresponding to the condition of an ideal voltage measurement. $Im\{U_S\}$ depends linearly on κ, as expected from Equation (1) [37]. The conductivity of the medium is varied between 1 S/m and 2 S/m, since this corresponds approximately to the conductivity of the blood [42]. This allows the sensitivity S_κ of the differential transformer to be determined in terms of the conductivity κ as input variable according to Equation (3).

$$S_\kappa = \frac{dIm\{U_S(\kappa)\}}{d\kappa} = \frac{Im\{U_S(\kappa_2) - U_S(\kappa_1)\}}{\kappa_2 - \kappa_1} \tag{3}$$

For all following sections, the coordinate system is defined as shown in Figure 3. The z-axis points in the longitudinal direction, i.e., along the ferrite core. The x- and y-axis point in radial direction.

Figure 3b shows a cross-section of the differential transformer in the y-z-plane. Depending on the parameter of interest, here, the height h_M in z-direction or the outer radius $r_{M,outer}$ of the medium in x-y-direction are varied. In Section 3.1.2, the radius $r_{S,outer}$ of L_{S1} and L_{S2} are also changed.

3. Results and Discussion

3.1. Impact of the Sample Geometry on the Sensitivity

An important issue that was not considered in previous investigations [18,37] and thus is not included in e.g., Equation (1), is the relationship between the sample geometry and the sensitivities S_κ and S_c and consequently the signal-to-noise ratio *SNR* of the differential transformer. Although other factors, such as the diameter or permeability of the ferrite core, also affect the sensitivity, in this work we will focus on rotationally symmetric samples as well as on the radius of the primary and secondary coils. Especially, the radius r_M and the height h_M and therefore the volume of the sample is of particular interest, since often, the sample volume is defined by certain specifications coming from the application. For example, such restrictions can be found in the continuous in-line monitoring of the sodium concentration of the blood in extracorporeal circuits during dialysis treatment, where, in addition to flow requirements, the sample volume should be kept as low as possible in order to draw as less blood as possible from the patient. Therefore, the effect of the height h_M and the outer radius $r_{M,outer}$ of a cylindrically shaped sample compartment on the sensitivities S_κ and S_κ and the *SNR* should be investigated. Thus, the objective is to determine to what degree an increase of these parameters can improve S_κ, S_c, and *SNR* while considering the sample volume limitations in order to derive design rules for the sample compartment.

Therefore, as illustrated in Figure 4, Section 3.1.1 deals with the investigation of the field distribution in the sample compartment in z-direction and Section 3.1.2 studies the impact of the radius of the sample compartment on the sensitivity and the signal to noise ratio *SNR*. First, in Section 3.1.1 a theoretical consideration of the depth of penetration of the field into the medium is given. Here, it is found that a case distinction must be made. If the ratio of the mean radius of the primary coil $r_{P,M}$ to the skin depth or standard depth of penetration δ_S is greater than 10, the equation for δ_S can be used to calculate the depth of penetration. This case is well known and already described in detail in the literature. Thus, no further consideration is made for this case. However, for most technically relevant liquids, the ratio $r_{P,M}/\delta_S$ is less than 10^{-1}. For this case, we present a new equation enabling the true depth of penetration to be determined. Then, this new equation is verified with the simulation model. In addition, the influence of the height of the medium h_M on the sensitivity S_κ is investigated. Subsequently, these results are validated experimentally and the influence of h_M on the signal-to-noise ratio *SNR* is investigated. In Section 3.1.2, first, the influence of the radius of the medium on the sensitivity is investigated by using simplified theoretic considerations. The limits

of this simplified theory are shown. Afterwards, for a more detailed consideration, the influence of the radius of the medium on the sensitivity is analyzed with the simulation model. These results are subsequently validated experimentally by measurements using the constructed differential transformer. In addition, the influence on the *SNR* is also investigated here. Since these findings show that the radius of the secondary coils affects the sensitivity curve, the simulation model validated by the experimental investigations is then used to evaluate this influence in detail. All the data shown in the following section are included in it. Further information on data availability can be found in the Supplementary Materials statement. The data presented in this study are available on request from the corresponding author.

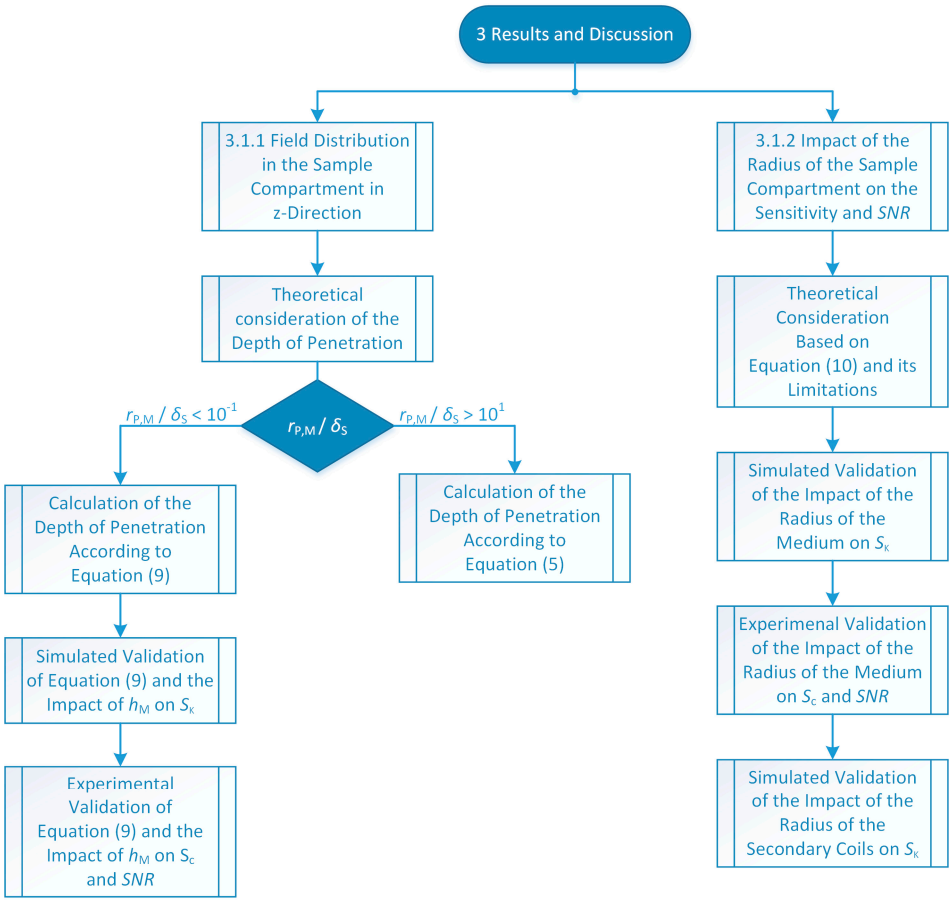

Figure 4. Flowchart of the investigations conducted in Section 3.

3.1.1. Field Distribution in the Sample Compartment

The magnitude of the electromagnetic field generated by the excited primary coil L_P decreases in z-direction. As the density of the eddy and displacement currents I_M, measured by the secondary coils L_{S1} and L_{S2}, are directly related to the electromagnetic field inside the medium according to Maxwell's law [43], the current density within the medium also decreases along the z-direction. Thus, above a certain height h_M of the sample compartment, the induced current density is too low for a measurable contribution to the secondary magnetic field and hence to the output voltage U_S. Therefore, a further increase of h_M does not improve sensitivity. The penetration depth of electromagnetic field and thus the eddy currents in the sample is typically described by solving the field diffusion equation of a planar electromagnetic wave, propagating e.g., in z-direction and reaching a

conducting half space at $z = 0$. Solving this diffusion equation results in Equation (4) [43–45], where this is valid for $z \geq 0$. For $z < 0$, $J(z)$ is zero.

$$J(z) = J(0) \cdot e^{-\frac{z}{\delta_S}} \tag{4}$$

Here, $J(z)$ is the current density depending on the distance in z-direction. $J(0)$ is the initial value of the current density for $z = 0$. By replacing J with the magnetic field B or electrical field E, Equation (4) also describes the decrease of this parameter inside a medium. For eddy current sensors, the parameter δ_S is typically called standard depth of penetration or skin depth in the scientific literature [46]. At $z = \delta_S$ the current density has attenuated to $1/e$ or about 37% respectively of the initial value at $z = 0$. The standard depth of penetration δ_S only depends on material parameters such as the conductivity κ and the permeability μ as well as frequency f of the field and can be calculated according to Equation (5) [43].

$$\delta_S = \sqrt{\frac{1}{\pi f \mu \kappa}} \tag{5}$$

For typical applications of the differential transformer, the conductivity measured in Siemens per meter is in the single-digit range. For example, the conductivity of blood for monitoring the sodium concentration is between 1 S/m and 2 S/m [42]. In the case of water quality monitoring, the conductivity can be slightly higher, e.g., about 5 S/m for seawater [47]. The magnetic properties μ of a sample is the product of the permeability of free space μ_0 and the relative permeability μ_r of the corresponding medium, where usually for the application presented here the relative permeability can be considered as $\mu_r = 1$, so that $\mu = \mu_0$ applies. For a differential transformer driven at a frequency f of 155 kHz, Equation (5) would yield a standard depth of penetration δ_S of about 0.9 m to 1.3 m for conductivities between 1 S/m and 2 S/m, respectively. However, these depths of penetration are not to be expected in practical applications.

In order to calculate the true depth of penetration δ_T, Dodd et al. has described the depth of penetration of an eddy current sensor for non-destructive material testing using an analytical solution of the vector potential A [48]. The excited coil is an axisymmetric circular coil with a rectangular cross-section in the plane of the symmetry axis and radial axis. The mean coil radius $r_{P,M}$ is the arithmetic mean value between the outer and inner radius of the coil. Since these sensors have similarities to the differential transformer with respect to the depth of penetration, the findings can be transferred. The very complex description using the vector potential A was analyzed by Mottl [49]. It was found that a calculation of the standard depth of penetration δ_S according to Equation (5) is valid as long as the ratio between the mean coil radius $r_{P,M}$ of the excited coil and the calculated standard depth of penetration δ_S is greater than 10 ($r_{P,M}/\delta_S > 10$). For a smaller ratio, the actual depth of penetration deviates from that in Equation (5). The reason is the assumption of planar waves to derive Equation (4). A planar wave implies, among other things, that the electromagnetic field has a constant amplitude along the propagation direction and is not attenuated without the presence of a medium. The attenuation of planar waves is solely due to the properties of the medium. To obtain an understanding why the true depth of penetration δ_T can be significantly lower and to have a much easier approach to estimate the δ_T than in [48], we use the Biot–Savart law. This allows to determine the magnetic field $B(z)$ of a coil that is rotationally symmetric to the z-axis, along the z-direction. Since the Biot–Savart law neglects the spatial expansion of the coil, it is assumed for a coil with a rectangular cross-section that all n_P windings are concentrated at the mean radius $r_{P,M}$. In this case, the $B(z)$-field along the symmetry axis (z-axis) of a coil excited with the current I_P can be described by Equation (6).

$$B_P(z) = \frac{\mu}{2} \frac{r_{P,M}^2 \, I_P \, n_P}{\left(r_{P,M}^2 + z^2\right)^{\frac{3}{2}}} \tag{6}$$

Equation (6) shows that the *B*-field decreases with increasing distance z from coil origin ($z = 0$). The decrease depends on the mean coil radius $r_{P,M}$. Calculating the *B*-field of a coil in free space and without the presence of any sample according to Equation (6) at the position $z = \delta_S$ and normalizing the *B*-field to the initial value of the *B*-field at the position $z = 0$, yields Equation (7).

$$\frac{B_P(\delta_S)}{B_P(0)} = \left(\frac{1}{1 + \left(\frac{\delta_S}{r_{P,M}} \right)^2} \right)^{\frac{3}{2}} \tag{7}$$

By plotting Equation (7) versus the ratio $r_{P,M}/\delta_S$, Figure 5 is obtained, where $r_{P,M}/\delta_S$ can be varied by changing the primary coil radius $r_{P,M}$ and the standard depth of penetration δ_S depending on the sample conductivity and the excitation frequency according to Equation (5).

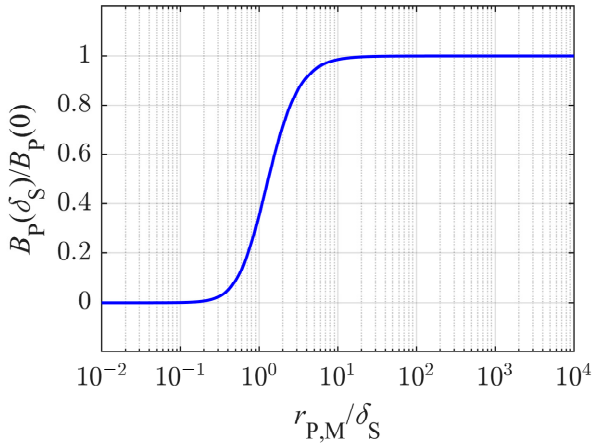

Figure 5. Ratio of the magnetic field strength B_P of the primary coil at the point $z = \delta_S$ to the initial field strength at the point $z = 0$ versus the ratio of the mean primary coil radius $r_{P,M}$ to δ_S. δ_S is the standard depth of penetration calculated according to Equation (5) to determine the skin depth of planar waves within a medium.

For values of $r_{P,M}/\delta_S \geq 10$, it can be seen that the ratio $B_P(\delta_S)/B_P(0)$ tends towards the value 1, meaning that the *B*-field in free space can be seen almost constant up to $z = \delta_S$, meeting the conditions to be considered as a planar wave and supporting the results obtained from [49]. Hence, the attenuation within the medium can be described by Equations (4) and (5), as the medium is the dominant reason for lowering the current density or field strengths. To reach the standard depths of penetration δ_S of about 1 m for the above-calculated sodium monitoring in blood would require a technically unreasonable coil radius of about 10 m. The mean coil radius $r_{P,M}$ of the differential transformer used here is about 9.55 mm, giving a ratio $r_{P,M}/\delta_S$ of about 10^{-2}. At this point, Equation (7) approaches zero, indicating that the *B*-field of the coil has nearly decreased to zero at $z = \delta_S$ (with $\delta_S \approx 1$ m) only due to the coil geometry. Thus, it can be assumed that the decrease of the field is dominated by the coil geometry of the excited coil while the attenuation due to the electromagnetic properties of the medium has a negligible impact on the field distribution. In order to estimate the true depth of penetration δ_T in the case that the decrease of the *B*-field is dominated by the coil geometry, we present a very simple approach using the Biot–Savart law. δ_T is defined similar to δ_S as the depth of penetration, at which the *B*-field and thus also the current density J has declined to the value $1/e$ i.e., 37% relative to the initial value at $z = 0$. Therefore, the ratio $B_P(\delta_T + d_0)/B_P(d_0)$ is determined by using Equation (6) and is set equal to $1/e$. d_0 is the distance in z-direction between the primary coil and the medium, see Figure 3, and is about 11.25 mm for the differential transformer used here. As a result, Equation (8) is obtained.

$$\frac{B_P(\delta_T + d_0)}{B_P(d_0)} = \frac{1}{e} = \frac{\mu \cdot r_{P,M}^2 \cdot I_P}{2\left(r_{P,M}^2 + (\delta_T + d_0)^2\right)^{\frac{3}{2}}} \cdot \frac{2\left(r_{P,M}^2 + d_0^2\right)^{\frac{3}{2}}}{\mu \cdot r_{P,M}^2 \cdot I_P} = \left(\frac{r_{P,M}^2 + d_0^2}{r_{P,M}^2 + (\delta_T + d_0)^2}\right)^{\frac{3}{2}} \quad (8)$$

Solving Equation (8) for the true depth of penetration δ_T leads to Equation (9), enabling the depth of penetration of eddy current sensors to be estimated in a simple way. This equation is valid for $r_{P,M}/\delta_S < 10^{-1}$, since here the decrease of the field strength of the B-field is mainly caused by the coil geometry and the attenuation due to the medium can be neglected.

$$\delta_T = \sqrt{\left(\left(r_{P,M}^2 + d_0^2\right) \cdot e^{\frac{2}{3}} - r_{P,M}^2\right)} - d_0 \quad (9)$$

Calculating the true depth of penetration δ_T for the differential transformer used here with $r_{P,M}$ = 9.55 mm and d_0 = 11.25 mm, Equation (9) results in δ_T = 7 mm, which is significantly lower than the δ_S of approximately 1 m due to the relatively low conductivity of the medium κ (e.g., blood) and excitation frequency f according to Equation (5).

In order to confirm the calculated δ_T, numerical computer simulations are conducted using the CST-EM Studio model described in Section 2.3. Subsequently, these simulations are validated by measurements. Besides the true depth of penetration δ_T of the eddy currents and the resulting current distribution of the current density J_M within the medium, the dependence of the sensitivity on the height h_M of the medium is of particular interest. Since the sensitivity is proportional to the total eddies and displacement currents I_M induced into the medium, i.e., to the integral of J_M along the z-axis and J_M decreases with increasing h_M, it can be expected that S_κ initially rises with increasing height h_M of the medium and starts to saturate at a certain point. As the eddy current density has decreased to 37% of the initial value at δ_T, the sensitivity S_κ can only increase by 37% by further increasing h_M, i.e., S_κ has reached 67% of the maximum value. Considering an exponentially decreasing depth of penetration, the point $3{\cdot}\delta_S$ is called the effective depth of penetration. At this point, the current density is already attenuated by about 95%. Therefore, all currents induced above the effective depth of penetration have only a negligible effect. The definition of the effective depth of penetration is also assumed here for the true depths of penetration determined according to Equation (9), so that $3{\cdot}\delta_T$ applies to the effective depth of penetration. A calculated true depth of penetration δ_T of 7 mm, results in an effective depth of penetration $3{\cdot}\delta_T$ = 21 mm.

Now, simulations according to the model from Section 2.3 help to verify whether this relationship between the true depths of penetration of the current density is consistent with the dependence of sensitivity on the height h_M of the medium or sample compartment, respectively. First, the height h_M of the sample compartment is set to 50 mm, the outer radius $r_{M,outer}$ to 47 mm and the inner radius to 0 mm. The conductivity κ of the medium is set to 2 S/m and the primary coil is excited with 1 V_{PP} and 155 kHz. Figure 6 shows the resulting curve of the current density within the sample in z-direction (orange solid line versus the upper x-axis, normalized to the initial J_M at the bottom of the medium). The intersection of the horizontal black dotted line at 0.37 with the vertical black dotted line gives a simulated true depth of penetration of δ_T = 7.4 mm. The height h_M of the medium is now varied from 0 mm to 50 mm, in order to proof that the depth of penetration can also be determined based on the sensitivity of the differential transformer. Each height h_M is simulated for 1 S/m and 2 S/m, allowing the sensitivity to be determined using Equation (3). The simulated sensitivity S_κ is shown in Figure 6 (blue solid line versus the lower x-axis). The sensitivity is normalized to the maximum $S_{\kappa,max}$ of 114.8 µV/S/m. As can be seen, the sensitivity first rises rapidly with increasing h_M and then saturates, as expected. 63% of the maximum sensitivity $S_{\kappa,max}$, is reached at the simulated δ_T of the induced current density J_M is 7.4 mm. Thus, the true depth of penetration δ_T of the eddy and displacement currents and the sensitivity S_κ of the differential transformer are proportional to each other, and δ_T can therefore be derived from the sensitivity, which is

a considerable advantage for determination of δ_T by measurements, since the sensitivity is much easier to measure than J_M within the medium. This simulated true depth of penetration δ_T is close to the calculated δ_T of 7 mm by Equation (9), which is also shown as the green dashed line in Figure 6.

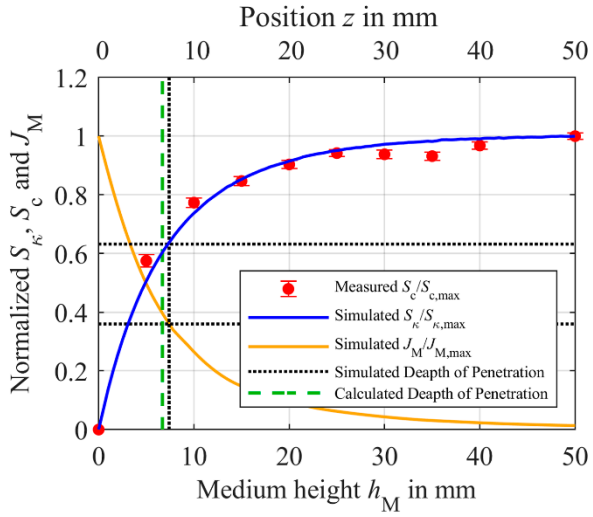

Figure 6. Normalized simulated sensitivity S_κ (blue solid line) of the differential transformer depending on the height h_M of the medium (lower x-axis), if h_M is changed from 0 mm to 50 mm (conductivity κ of the medium: 1 S/m to 2 S/m). The red dots are the measured sensitivity S_c with error bar, when h_M (lower x-axis) is varied from 0 mm to 50 mm in 5 mm steps (the sodium concentration is 100 mmol/L and 150 mmol/L). S_κ is normalized to the maximum sensitivity $S_{\kappa,max}$ = 114.8 µV/S/m. The measured sensitivity S_c and the error bars are both normalized to $S_{c,max}$ = 38.74 mV/mol/L. The orange line represents the current distribution J_M in z-direction (upper x-axis) within the sample with h_M = 50 mm and a conductivity of κ = 2 S/m normalized to the maximum $J_{M,max}$ of 202.5 mA/m^2. The true depth of penetration δ_T obtained from the simulations, at which the sensitivity has reached about 63% or J_M as decreased to 37% of its maximum value, is 7.4 mm (vertical black dotted line). The true depth of penetration δ_T calculated using Equation (9) is at 7 mm (green dashed line).

In order to validate the simulations, the depth of penetration was also measured, using the differential transformer described in Section 2.1. The differential transformer is driven with a peak-to-peak input voltage of 1 V_{pp} and a frequency f of 155 kHz. The medium was positioned above the differential transformer within a compartment having a radius of 47 mm. Similar to the simulation; the medium height h_M was varied from 0 mm to 50 mm. As described in Section 2.2, the sample solution is DI-water containing NaCl with a concentration of c_1 = 100 mmol/L and c_2 = 150 mmol/L, so that the sensitivity S_c can be calculated according to Equation (2) for each height h_M. The results are shown in Figure 6 as red dots. The measured sensitivity is normalized to the maximum measured $S_{c,max}$ of 38.74 mV/mol/L. The measured values are in good agreement with the simulated values validating the simulation and the mathematical model from Equation (9).

Furthermore, an important issue is whether the increased sensitivity can improve the precision and thus the *SNR* of the differential transformer. Therefore, we determined the noise of the output signal by the standard deviation of the imaginary part of U_S, which is averaged 512 times giving a measured value about every 11 s. Table 1 gives the noise measured for different heights h_M and a concentration of 150 mmol/L NaCl. The standard deviation of the measured concentration can be calculated by the standard deviation of $Im\{U_S\}$ divided by the respective sensitivity S_c. Table 1 reveals that there is no correlation between h_M and the noise of the imaginary part of U_S. Thus, comparing the standard deviation of c_{std} can be reduced from 0.81 mmol/L to 0.44 mmol/L by increasing h_M due

to the increasing sensitivity S_c. The relative error bars normalized to $S_{c,max}$ are illustrated in Figure 6.

Table 1. Measured standard deviation of the output voltage $Im\{U_S\}$ of the differential transformer, corresponding sensitivity S_c and the resulting standard deviation of the measured concentration c_{std} depending on the height h_M of the medium. The experimental measured data are included in Figure 6 (red).

h_M in mm	Standard Deviation of $Im\{U_S\}$ in µV	S_c in mV/mol/L	Standard Deviation of c_{std} in mmol/L
0	18.82	0	-
5	18.07	22.28	0.81
10	18.43	29.69	0.62
15	19.65	32.82	0.60
20	19.02	35.00	0.54
25	17.26	36.50	0.47
30	20.36	36.34	0.56
35	19.52	36.10	0.54
40	18.88	37.50	0.50
50	17.10	38.74	0.44

In summary, the true depth of penetration δ_T of the differential transformer used here cannot be calculated using Equation (5) due to the small ratio $r_{P,M}/\delta_S$ of the primary coil radius to the standard depth of penetration. As a result of the relatively small coil radius $r_{P,M}$ and the low conductivity of the medium, the magnetic field of the coil and thus the currents induced into the medium have already approached zero before reaching δ_S due to the coil properties. δ_S only depends on the frequency f of the excited coil and the material properties of the medium, such as the conductivity κ and permeability μ. Therefore, we introduced Equation (9) estimating the true depth of penetration δ_T when $r_{P,M}/\delta_S$ is below 10^{-1}. With Equation (9), the true depth of penetration δ_T of the differential transformer used here, was calculated to 7 mm. The simulation model, validated by measurements, showed a depth of penetration of about 7.4 mm. Hence, Equation (9) is well suited for estimating δ_T. The true depth of penetration δ_T is particularly important for the design of the measuring chamber, when the sample volume is limited by the application. For $h_M \leq \delta_T$, the sensitivity can be significantly improved by increasing h_M. However, by further increasing h_M the effect of h_M on S_κ and S_c decreases, e.g., for $h_M > 3 \cdot \delta_T$, increasing h_M does not noticeably increase the sensitivity. Since the noise of the output signal $Im\{U_S\}$ has shown no inherent correlation with the medium height h_M, an increase in sensitivity by increasing h_M is associated with an improvement in signal-to-noise ratio *SNR*.

3.1.2. Impact of the Radius of the Sample Compartment on the Sensitivity

In this section, the impact of the radius of the sample compartment and thus the radius r_M of the medium is discussed. In [37], we have derived Equation (10) in order to improve the sensitivity of the differential transformer by an optimized distance d_{PCB} between the three planar PCB coils, see Figure 3. This mathematical model can be used to increase the sensitivity and the signal-to-noise ratio *SNR* by optimizing the magnetic coupling between the coils and the medium.

$$S_\kappa \sim \frac{C n_S n_P r_{M,M}^2}{L_P \left(r_{P,M}^2 + (d_{PCB} + d_M)^2 \right)^{\frac{3}{2}}} \left(\frac{1}{\left(r_{M,M}^2 + d_M^2 \right)^{\frac{3}{2}}} - \frac{1}{\left(r_{M,M}^2 + (2d_{PCB} + d_M)^2 \right)^{\frac{3}{2}}} \right) \quad (10)$$

d_M is the distance between the medium and the upper secondary coil L_{S1}, see Figure 3. The factor C summarizes further constants as well as geometrical factors of the ferrite core, the angular frequency and the primary voltage, which will not be discussed here

any further. Considering Equation (10), additional to the distance d_{PCB} the mean medium radius $r_{M,M}$ is relevant. $r_{M,M}$ is defined as the geometric mean value between the inner radius $r_{M,inner}$ and the outer radius $r_{M,outer}$ of the cylindrically shaped sample compartment, representing the boundaries of the medium. Plotting Equation (10) for $r_{M,inner}$ = 0 mm versus $r_{M,outer}$ and setting a distance d_{PCB} between the PCB coils to 8 mm and d_M to 1 mm leads to Figure 7. Setting $r_{M,inner}$ to zero yields $r_{M,outer} = 2 \cdot r_{M,M}$.

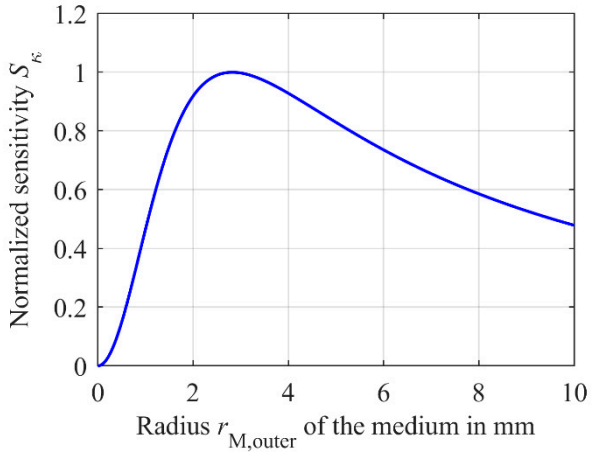

Figure 7. Calculated sensitivity S_κ of the differential transformer using Equation (10) normalized to the maximum sensitivity depending on the outer radius $r_{M,outer}$ of the medium. If the inner radius $r_{M,inner}$ of the medium is set to zero, $r_{M,outer} = 2 \cdot r_{M,M}$ applies. The distance d_{PCB} between the PCB coils is 8 mm, the distance d_M between the medium and the upper secondary coil L_{S1} is 1 mm.

For deriving Equation (10), the medium was considered as a coil with one winding carrying the total induced eddy and displacement currents I_M at $r_{M,M}$ and thus causing a secondary field B_S. Hence, B_S can be determined by using the Biot–Savart law according to Equation (6) [37] and Figure 7 and therefore Equation (10) can be interpreted accordingly. First, the amplitude of the secondary field B_S increases squared to radius $r_{M,M}$. Thus, the factor $r^2_{M,M}$ in Equation (10) dominates the influence on the sensitivity S_κ for small radii, leading to an increased sensitivity increasing $r_{M,M}$. However, at a certain value of $r_{M,M}$, the secondary field reaches the lower secondary coil L_{S2}, see Equation (6), resulting in a progressive penetration of B_S of both secondary coils L_{S1} and L_{S2} with increasing $r_{M,M}$. Hence, a reduction of S_κ can be observed. The loss of sensitivity due progressive penetration of B_S of both secondary coils L_{S1} and L_{S2} is described in Equation (10) by the term in parentheses. However, Equation (10) only considers the geometrical effect of $r_{M,M}$. The total current intensity of the eddy and displacement currents I_M was determined in [37] using Faraday's law and the total impedance Z_M of the medium. The dependence of Z_M on the height h_M and the mean radius $r_{M,M}$ of the medium was neglected. Furthermore, the complex distribution of the primary field B_P was simplified and assumed to be just oriented in positive z-direction within the ferrite core. These simplifications leads to a constant induced current I_M within the medium independent of the radius $r_{M,outer}$. A constant current I_M independent of the radius would imply a current density J_M evenly distributed along the radius r_M. The amplitude of J_M changes as a function of $r_{M,outer}$. However, the current I_M is expected to grow progressively with increasing size of the medium as Z_M decreases. After a certain value of $r_{M,outer}$, less current is induced in the outer area with a large radius of the medium due to the complex field distribution of B_P. As a result, the current I_M should saturate.

Therefore, using the differential transformer model from Section 2.3, we simulate the current distribution J_M within the medium at a conductivity κ of the medium of 2 S/m at an excitation of the primary coil of 1 V_{PP} and a frequency of 155 kHz. Figure 8a shows a cross sectional view in the x-y-plane from the top. The simulated current density is represented by arrows and rotates around the z-axis. The color gradient indicates the intensity of J_M.

Figure 8b shows a cross sectional view in the *y*-*z*-plane. Again, the intensity J_M is given by the color gradient.

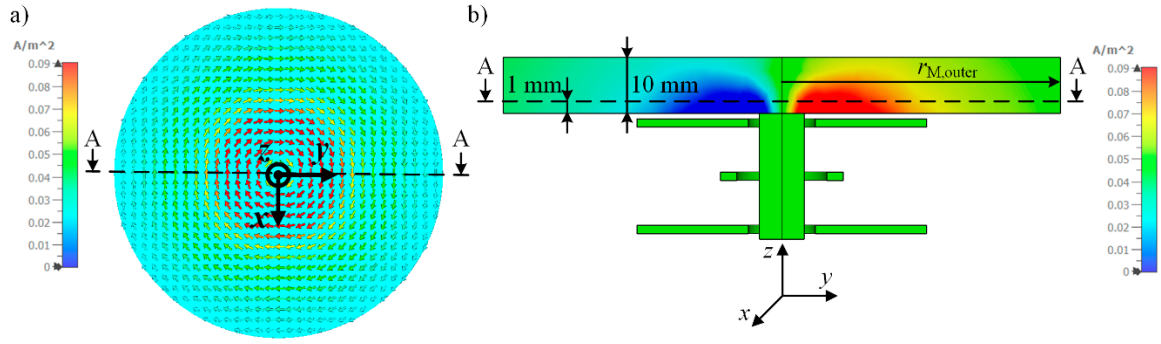

Figure 8. Simulation of the distribution of the current density J_M within the medium. The total height h_M is 10 mm and the outer radius $r_{M,outer}$ is 50 mm. The primary coil is excited with 1 V_{PP} at 155 kHz. (**a**) The top view shows a cross section at a height of 1 mm in *z*-direction through the medium in the *x*-*y*-plane. J_M is represented by arrows. (**b**) Cross sectional view in the *y*-*z* plane. The intensity of J_M is color-coded.

Figure 9 shows the resulting current density distribution $J_{M,x}$ of the *x*-component of the induced eddy and displacement current densities along the cutting line A-A located at a height of 1 mm inside the medium as depicted in Figure 8. The outer radius $r_{M,outer}$ of the medium is 200 mm (Figure 9, red solid line) and 50 mm (Figure 9, blue dotted line), respectively, and the height h_M is 10 mm. These parameters represent the boundaries of the sample compartment.

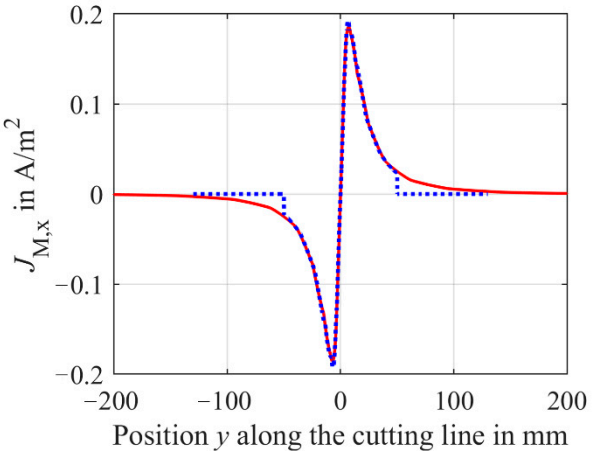

Figure 9. Simulated current density distribution $J_{M,x}$ of the *x*-component of the induced eddy and displacement current densities along the cutting line A-A located at a height of 1 mm within the medium. For the simulations, the basic setup of the simulation model from Section 2.3 is used. The cutting line A-A is depicted in Figure 8. The total height h_M of the medium is 10 mm and the conductivity is 2 S/m. The blue dotted line shows $J_{M,x}$ for an outer radius $r_{M,outer}$ of the medium of 50 mm and the red solid line for $r_{M,outer}$ = 200 mm. $r_{M,outer}$ represents the boundaries of the sample compartment in radial direction.

Figure 9 reveals a point symmetry of the current density $J_{M,x}$ to the origin, representing the center of the radially symmetric medium. Starting from the origin of the medium (x = y = 0 mm), the absolute value of the current density increases with increasing radius r_M and reaches a maximum at about 7 mm. Then, the absolute current density decreases until $J_{M,x}$ approaches zero. Comparing the current densities $J_{M,x}$ for sample boundaries of $r_{M,outer}$ = 50 mm and $r_{M,outer}$ = 200 mm, the current density $J_{M,x}$ is almost independent of $r_{M,outer}$ until the outer boundary $r_{M,outer}$ is reached. Beyond this boundary, it is evident

that the current is forced to zero. Hence, the initial assumption for Equation (10) of a evenly distributed J_M along the radius with an amplitude depending on the boundary of the sample compartment $r_{M,outer}$ is not fulfilled. Thus, the total current of the induced eddy and displacement currents I_M is also not constant for different radii of the medium as long as J_M has not fully decreased to zero for very high $r_{M,outer}$. Furthermore, a possible influence of different radii $r_{S,outer}$ of the secondary coils L_{S1} and L_{S2} is not considered in this Equation (10).

In order to determine the exact impact of the radius $r_{M,outer}$ and of the outer radius $r_{S,outer}$ of the secondary coils on the sensitivity, simulations are executed using the model from Section 2.3, followed by validation of the model via measurements. As for the previous simulations of the current distribution, h_M is set to 10 mm. The outer radius $r_{M,outer}$ of the medium is varied from 0 mm to 100 mm. In order to determine the sensitivity S_κ according to Equation (3), each step is simulated at a conductivity of κ = 1 S/m and κ = 2 S/m. The inner radius $r_{M,inner}$ is fixed to zero. The results are shown in Figure 10 as a blue solid line, normalized to the maximum sensitivity of 88 µV/S/m. As expected, the simulation shows an increasing sensitivity with increasing radius $r_{M,outer}$. However, at a certain value, S_κ saturates and does not decrease.

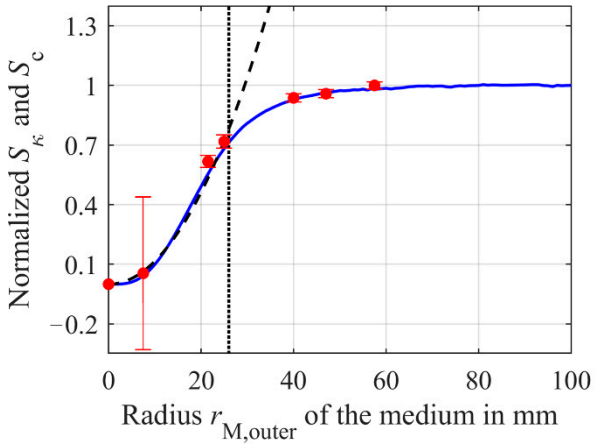

Figure 10. Simulated sensitivity S_κ (blue solid line) normalized to $S_{\kappa,max}$ of 88 µV/S/m and measured sensitivity S_c (red dots) with error bars of the sensor noise translated into a concentration c_{std}, both normalized to $S_{c,max}$ of 30.98 mV/mol/L versus the outer radius $r_{M,outer}$ of the medium. The basic setups from Sections 2.1 and 2.3 were used for the measurements and simulation, respectively. To determine S_κ, the conductivity of the medium in the simulation model was varied between 1 S/m and 2 S/m. S_c was determined via measurements by two different NaCl concentration within the medium (100 mmol/L and 150 mmol/L). The height h_M of the medium was 10 mm. The outer secondary coil radius $r_{S,outer}$ was 26 mm in both cases and is shown as a black dotted line. The increase of S_κ and S_c up to $r_{S,outer}$ can be well approximated by a quadratic function (black dashed line).

A possible reason for the sensitivity S_κ not decreasing after a certain radius $r_{M,outer}$ as shown in Figure 7 could be the more complex shape of the current density J_M within the medium. For larger radii of $r_{M,outer}$, J_M decreases towards zero after its maximum at about 7 mm and thus contributes less to the secondary field B_S. In addition, due to the inhomogeneous distribution of J_M, the mean radius $r_{M,M}$ of the medium cannot be calculated simply from the geometric mean value of $r_{M,inner}$ and $r_{M,outer}$. As J_M decreases for larger $r_{M,outer}$, $r_{M,M}$ increases much slower than expected, causing less penetration of B_S into the lower secondary coil L_{S2}, as B_S does not extend that far along the z-direction, see Equation (6). This results in a saturation of S_κ instead of a reduction for larger $r_{M,outer}$. For small $r_{M,outer}$, the simulated characteristic of the sensitivity of the differential transformer corresponds in good approximation to the expected behavior shown in Figure 7 and can therefore be approximated well by a quadratic function $f(r_{M,outer}) = a \cdot r^2_{M,outer}$ (Figure 10, black dashed line). Fitting in the range of $r_{M,outer}$ = 0 mm to $r_{M,outer}$ = 26 mm leads to

$a = 102.4 \times 10^{-6}$ mVS/(mol·mm^2) having a coefficient of determination R^2 of 0.9925. For $r_{M,outer} > 26$ mm, $f(r_{M,outer})$ increasingly deviates from S_κ. This value of $r_{M,outer}$ is indicated by the black dotted line in Figure 10 and represents the outer radius $r_{s,outer}$ of the secondary coils L_{S1} and L_{S2}. The impact of the secondary coil radius $r_{S,outer}$ will be investigated in more detail later. First, the simulation results have to be validated by measurements.

Therefore, similar to Section 3.1.1, the differential transformer described in Section 2.1 is driven with a voltage U_P of 1 V_{PP} at a frequency f of 155 kHz. The medium is placed above the differential transformer and is located in sample compartments with fixed height h_M of 10 mm and variable diameters of 15 mm, 43 mm, 50 mm, 80 mm, 94 mm, and 115 mm. The sample solutions inside the compartments contain NaCl with concentrations of c_1 = 100 mmol/L and c_2 = 150 mmol/L, enabling the calculation of sensitivity S_c for each radius. The measured results are normalized to the maximum sensitivity of S_c = 31 mV/mol/L and are shown in Figure 10 as red dots. As can be seen, the results correspond well with the simulations, meaning the simulation model can be considered as validated. Similar to the simulations, the sensitivity initially increases with increasing radius of the medium. As in Section 3.1.1, we also investigate whether the precision can be enhanced by the increased sensitivity. Therefore, the noise of the output voltage was determined by the standard deviations of $Im\{U_S\}$ at different radii $r_{M,outer}$. The results can be found in Table 2. Table 2 reveals no correlation between the noise and $r_{M,outer}$. The standard deviation of the concentration c_{std} was calculated by dividing the standard deviation of $Im\{U_S\}$ by the respective sensitivity S_c. Due to the initial low sensitivity at r_M = 7.5 mm, the standard deviation of concentration c_{std} is 11.9 mmol/L. Comparing this to a radius of 57 mm, c_{std} is only 0.57 mmol/L, which is a significant improvement in the precision of the differential transformer. The relative error bars normalized to $S_{c,max}$ are also illustrated in Figure 10.

Table 2. Measured standard deviation of the output voltage $Im\{U_S\}$ of the differential transformer, corresponding sensitivity S_c and the resulting standard deviation of the measured concentration c_{std} depending on the outer radius $r_{M,outer}$ of the medium. The experimental measured data are included in Figure 10 (red).

$r_{M,outer}$ in mm	Standard Deviation of $Im\{U_S\}$ in µV	S_c in mV/mol/L	Standard Deviation of c_{std} in mmol/L
0	18.82	0	-
7.5	20.23	1.7	11.9
25	23.31	22.24	1.05
40	18.43	29.04	0.63
47	18.43	29.69	0.62
57	17.67	30.98	0.57

As already mentioned, the increase of both the simulated sensitivity S_κ as well as the measured sensitivity S_c saturate at an outer radius of the medium $r_{M,outer}$ of about 26 mm. This corresponds exactly to the outer radius $r_{S,outer}$ of the secondary coils L_{S1} and L_{S2}. Therefore, the validated simulation model is used to investigate how $r_{S,outer}$ affects S_κ and if there is a correlation between $r_{S,outer}$ and the saturation radius. In this simulation, $r_{S,outer}$ is used as parameter between 15 mm and 150 mm. Thereby, only the radius $r_{S,outer}$ of the secondary coils are changed. The number of windings n_S of L_{S1} and L_{S2} are kept constant at 542. This means, for example, that the windings at $r_{S,outer}$ = 15 mm spread over a much smaller area than at $r_{S,outer}$ = 150 mm. The results of this simulation are shown in Figure 11.

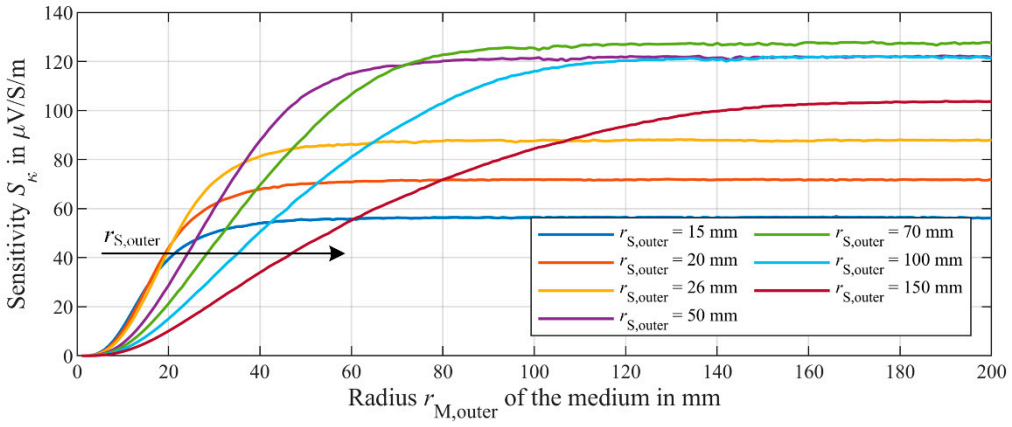

Figure 11. Dependence of the simulated sensitivity S_κ on the outer radius $r_{M,outer}$ of the medium at different outer secondary coil radii $r_{S,outer}$ of the secondary coils L_{S1} and L_{S2} as parameter. The height h_M of the medium is 10 mm. While changing $r_{S,outer}$, the number of windings of the secondary coils L_{S1} and L_{S2} are constant at 542 each.

As depicted in Figure 11, the initial increase of S_κ can approximated by a quadratic function $f(r_{M,outer}) = a \cdot r^2_{M,outer}$ for all secondary coil radii $r_{S,outer}$. However, for very large $r_{S,outer}$ of—e.g., 150 mm—a reasonable fit can only be realized up to $r_{M,outer}$ of about 40 mm, since the simulated S_κ increasingly deviates from $f(r_{M,outer})$ for larger $r_{M,outer}$. This is probably due to the increasing decline of J_M at larger radii. Furthermore, the simulations indicate a decrease of the initial slop of S_κ, i.e., the factor a of the quadratic function $f(r_{M,outer})$ becomes smaller, for larger secondary coil radii $r_{S,outer}$. Hence, the sensitivity curve is shifted towards larger medium radii $r_{M,outer}$ indicated by the arrow in Figure 11. A possible reason for this could be the reduction of the number of windings n_S of the secondary coils effectively involved in the magnetic coupling with the secondary field B_S. Since the divergence of magnetic fields must always be zero, the field lines are closed. The secondary field B_S propagates from the medium inside the ferrite core in negative z-direction, towards the secondary coils. At larger radial distance to the ferrite core, the field lines turn back in positive z-direction. The outer windings of the secondary coils with large $r_{S,outer}$ are thus penetrated by both the outgoing and returning field and causing a reduced net flux, so that no voltage is induced. These outer windings are effectively not involved in the coupling with the secondary field. By replacing the secondary inductance L_S with the proportionality $L_S \sim {n_S}^2$ in Equation (10), Equation (11) is obtained. Equation (11) indicates a dependency of the winding ratio between the primary coil n_P and the secondary coil n_S. Comparable to an ordinary transformer, lowering the effective n_S cause a reduction in the sensitivity.

$$S_\kappa \sim \frac{n_S}{n_P} \tag{11}$$

Nevertheless, the respective outer secondary coil radius $r_{S,outer}$ always corresponds very well with saturation radius regarding the sensitivity S_κ, meaning that there is a direct correlation between $r_{S,outer}$ and the saturation. A possible reason for this could be the reduced contribution of the circular currents with very large radius r_M to the secondary magnetic field B_S at the origin of the medium at x = y = 0 mm propagating over the ferrite core in negative z-direction. Equation (6) supports this assumption, since the contribution of the circular currents to B_S at the origin decreases with ${r_M}^{-1}$. However, leakage fields occur in the immediate surroundings of currents circulating at the outer boundary of the medium, although with decreasing amplitude due to the declining current density J_M. These leakage fields predominantly close directly around the current path and do not noticeably penetrate the ferrite core. Due to the small distance between the medium and the secondary coil L_{S1}, only L_{S1} is penetrated by these leakage fields. If the outer radius $r_{M,outer}$ of the medium exceeds the outer radius $r_{S,outer}$ of the secondary coil, such additional currents with larger radius r_M than $r_{S,outer}$ couple increasingly less with L_{S1},

leading to the saturation of the sensitivity. Therefore, an increase of $r_{S,outer}$ leads to more leakage fields being collected by L_{S1} and thus to an increased maximum sensitivity $S_{\kappa,max}$. This increase in maximum sensitivity $S_{\kappa,max}$ can be observed up to an $r_{S,outer}$ of 70 mm. However, for higher $r_{S,outer}$ $S_{\kappa,max}$ starts to decreases again as shown in Figure 12. Here, the maximum simulated sensitivity $S_{\kappa,max}$ is plotted versus the outer radius $r_{S,outer}$ of the secondary coils L_{S1} and L_{S2}.

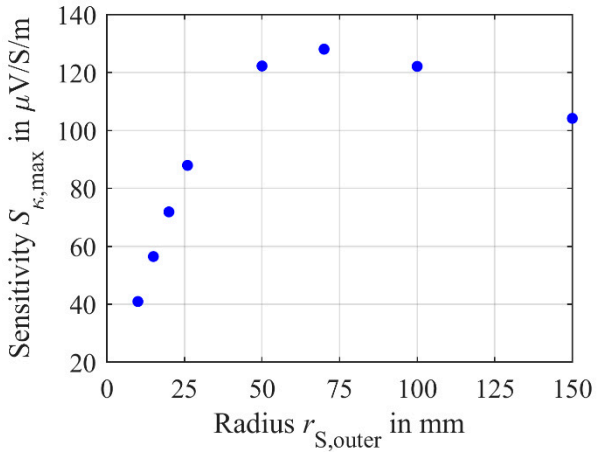

Figure 12. Maximum simulated sensitivity $S_{\kappa,max}$ versus the radius $r_{S,outer}$ of the secondary coils L_{S1} and L_{S2}.

Again, this decrease in the maximum sensitivity $S_{\kappa,max}$ for higher secondary radii $r_{S,outer}$ can be described by the reduction in the effective number of windings n_S involved in the coupling. At large radii, the current within the medium has nearly approached zero. Therefore, an increase of $r_{M,outer}$ has only a negligible effect, since almost no current exists. If the outer secondary coil radius $r_{S,outer}$ exceeds the radius in the medium where almost no current flows, the effective number of windings n_S is irrevocably reduced due to the same effect described before. Thus, to obtain an optimum design of the differential transformer in terms of sensitivity, the secondary coil radius $r_{S,outer}$ and radius of the medium must be carefully adjusted to each other. For example, a restricted radius $r_{M,outer}$ of the sample due to a limited sample volume needs a secondary coil radius close to $r_{M,outer}$. If $r_{M,outer}$ is not limited by the application, the secondary coil radius $r_{S,outer}$ have to be carefully adjusted to achieve high maximum sensitivity $S_{\kappa,max}$.

In the section above, the dependence of the sensitivities S_κ and S_c of the differential transformer on the radius of the medium has been analyzed. A good approximation of the initial increase of the sensitivities S_κ and S_c by increasing $r_{M,outer}$ with a quadratic function was found. Thus, an increase of $r_{M,outer}$ has significant impact on the sensitivity. For a constant number of windings of the secondary coils, the slope of this approximating function depends on the radius $r_{S,outer}$ of the secondary coil. Increasing $r_{S,outer}$ to $r_{S,outer} \geq r_{M,outer}$ results in the outer windings of the secondary coil not participating in the magnetic coupling between the medium and the secondary coil. Hence, the effective number of windings n_S of the secondary coil decreases, causing a decrease in sensitivity. The same effect of uncoupled windings n_S also occurs when $r_{S,outer}$ is increased over the radius where only negligible eddy and displacement currents circulate even for $r_{S,outer} < r_{M,outer}$. If the radius $r_{M,outer}$ of the medium exceeds the radius of the secondary coil, the sensitivity saturates, i.e., a further increase of $r_{M,outer}$ has no effect on S_κ and S_c. Thus, if $r_{M,outer}$ exceeds $r_{S,outer}$, the maximum sensitivity is reached. In experimental investigations, an increase of $r_{M,outer}$ seems useful, since the sensitivity significantly increases, but no correlation of the noise to $r_{M,outer}$ is observed. Thus, increasing the sensitivity by increasing $r_{M,outer}$ is a reasonable solution to improve the signal-to-noise ratio *SNR*.

4. Conclusions

In this work, we have investigated the influence of the sample compartment geometry on the sensitivities S_κ and S_c and the precision of a differential transformer. Therefore, we have addressed various design parameters with the use of the simulation software CST-EM Studios. The experimental investigations were conducted by using a PCB differential transformer.

First, the depth of field penetration was considered. The findings have revealed a variety of applications, where the standard depth of penetration δ_S or skin depth cannot be used to calculate the depth of penetration of the differential transformer as it is usually used for other eddy current sensors, e.g., for non-destructive material testing. Examples of these applications are continuous non-invasive monitoring of sodium concentration in blood, quality monitoring of liquids and monitoring of processes in bioreactors. Since the conductivity of the medium is relatively low here, only negligible attenuation occurs within the medium. Instead, the field characteristic of the exited primary coil is much more important. Thus, we have establish a new equation using the Biot–Savart law, allowing us to calculate the true depth of penetration δ_T of the differential transformer as a function of the mean primary coil radius $r_{P,M}$. This equation can be used as long as the ratio of $r_{P,M}$ to the standard depth of penetration δ_S is lower than 10^{-1}. The true depth of penetration δ_T calculated for the used PCB differential transformer is 7 mm. The depth of penetration determined by simulations and measurements is 7.4 mm. Thus, the simulated and measured δ_T is in good agreement with the calculated δ_T. Furthermore, the results show an increasing sensitivities S_κ and S_c by increasing the height h_M of the medium and thus the sample compartment up to $h_M = 3 \cdot \delta_T$, while the noise is not affected by h_M. Therefore, the signal-to-noise ratio *SNR* improves by increasing h_M. For example, converting the noise of the output signal of the differential transformer to a concentration, the standard deviation of the concentration can be reduced from 0.81 mmol/L at $h_M = 5$ mm to 0.44 mmol/L at $h_M = 50$ mm and thus improving the precision.

Secondly, the impact of the outer radius $r_{M,outer}$ of the medium and thus sample compartment was investigated. The results show an initial quadratic increase of the sensitivities S_κ and S_c with the radius $r_{M,outer}$. If $r_{M,outer}$ exceeds the outer radius $r_{S,outer}$ of the secondary coils, the sensitivities saturates, as from this point no relevant coupling exists between the additional secondary field B_S and the secondary coils. In general, the results reveal a complex interaction between the radius of the medium and the radius of the secondary coils. For instance, if the outer radius $r_{S,outer}$ of the secondary coil is larger than $r_{M,outer}$, or if the radius of the secondary coil is so large that no significant eddy and displacement currents are induced within the medium, the outer secondary coil windings are no longer involved in relevant magnetic coupling between the coil and the medium. Thus, the effective windings n_S of the secondary coils is reduced and consequently the sensitivity. As with the depth of penetration, increasing the sensitivity by increasing the radius of the medium and thus sample compartment the signal-to-noise ratio improves, since no correlation between the standard deviation of the noise and the radius of the medium was observed. For example, considering an outer radius of the medium of 7.5 mm, the standard deviation of the noise converted into a concentration is 11.9 mmol/L. In contrast, an outer radius of the medium of 57 mm results in a standard deviation of the noise converted into a concentration of only 0.57 mmol/L. Thus, by increasing the outer radius of the medium, the precision of the differential transformer can be significantly improved.

In future work, we will investigate whether a sample can also be characterized directly through a hose system (patent pending). In particular, the winding technique of the hose around an extended ferrite core could affect the sensitivity. The advantage of this approach would be in-line measurement of hose-guided samples without the need to leave the hose system and to be passed into a flow chamber.

Author Contributions: Conceptualization, M.B.; Methodology, M.B.; Validation, M.B. and A.Z.; Formal analysis, M.B.; Investigation, M.B. and A.Z.; Data curation, M.B. and A.Z.; Writing—original draft preparation, M.B.; Writing—review and editing, A.Z. and S.Z.; Visualization, M.B.; Supervision, S.Z.; Project administration, M.B. and S.Z.; Funding acquisition, S.Z. All authors have read and agreed to the published version of the manuscript.

Funding: This research received no external funding.

Institutional Review Board Statement: Not applicable.

Informed Consent Statement: Not applicable.

Data Availability Statement: The data presented in this study are available on request from the corresponding author.

Conflicts of Interest: The authors declare no conflict of interest.

References

1. Reinecke, T.; Biechele, P.; Sobocinski, M.; Suhr, H.; Bakes, K.; Solle, D.; Jantunen, H.; Scheper, T.; Zimmermann, S. Continuous noninvasive monitoring of cell growth in disposable bioreactors. *Sens. Actuators B Chem.* **2017**, *251*, 1009–1017. [CrossRef]
2. Lyu, Y.; Ji, H.; Yang, S.; Huang, Z.; Wang, B.; Li, H. New C4D Sensor with a Simulated Inductor. *Sensors* **2016**, *16*, 165. [CrossRef] [PubMed]
3. Gubartallah, E.A.; Makahleh, A.; Quirino, J.P.; Saad, B. Determination of Biogenic Amines in Seawater Using Capillary Electrophoresis with Capacitively Coupled Contactless Conductivity Detection. *Molecules* **2018**, *23*, 1112. [CrossRef]
4. Brito-Neto, J.G.A.; da Silva, J.A.F.; Blanes, L.; do Lago, C.L. Understanding Capacitively Coupled Contactless Conductivity Detection in Capillary and Microchip Electrophoresis. Part 2. Peak Shape, Stray Capacitance, Noise, and Actual Electronics. *Electroanalysis* **2005**, *17*, 1207–1214. [CrossRef]
5. Zhang, X.-Y.; Li, Z.-Y.; Zhang, Y.; Zang, X.-Q.; Ueno, K.; Misawa, H.; Sun, K. Bacterial Concentration Detection using a PCB-based Contactless Conductivity Sensor. *Micromachines* **2019**, *10*, 55. [CrossRef]
6. Parra, L.; Sendra, S.; Lloret, J.; Bosch, I. Development of a Conductivity Sensor for Monitoring Groundwater Resources to Optimize Water Management in Smart City Environments. *Sensors* **2015**, *15*, 20990–21015. [CrossRef]
7. Reinecke, T.; Biechele, P.; Frickhöffer, M.; Scheper, T.; Zimmermann, S. Non-Invasive Online Monitoring of Cell Growth in Disposable Bioreactors with a Planar Coil. *Procedia Eng.* **2016**, *168*, 582–585. [CrossRef]
8. Danisi, A.; Masi, A.; Losito, R. Performance Analysis of the Ironless Inductive Position Sensor in the Large Hadron Collider Collimators Environment. *Sensors* **2015**, *15*, 28592–28602. [CrossRef]
9. Loughlin, C. *Sensors for Industrial Inspection*; Springer: Dordrecht, The Netherlands, 1993; ISBN 978-94-010-5211-5.
10. Usher, M.J. *Sensors and Transducers*; Macmillan Education: London, UK, 1985; ISBN 978-0-333-38710-8.
11. Petchmaneelumka, W.; Koodtalang, W.; Riewruja, V. Simple Technique for Linear-Range Extension of Linear Variable Differential Transformer. *IEEE Sens. J.* **2019**, *19*, 5045–5052. [CrossRef]
12. Fraden, J. *Handbook of Modern Sensors*; Springer: New York, NY, USA, 2010; ISBN 978-1-4419-6465-6.
13. Santhosh, K.V.; Roy, B.K. A Smart Displacement Measuring Technique Using Linear Variable Displacement Transducer. *Procedia Technol.* **2012**, *4*, 854–861. [CrossRef]
14. Woolfson, A.D.; McCafferty, D.F.; Gorman, S.P.; McCarron, P.A.; Price, J.H. Design of an apparatus incorporating a linear variable differential transformer for the measurement of type III bioadhesion to cervical tissue. *Int. J. Pharm.* **1992**, *84*, 69–76. [CrossRef]
15. Degli Agosti, R.; Jouve, L.; Greppin, H. Computer-assisted measurements of plant growth with linear variable differential transformer (LVDT) sensors. *Arch. Sci.* **1997**, *50*, 233–244.
16. Aellig, W.H. A new technique for recording compliance of human hand veins. *Br. J. Clin. Pharmacol.* **1981**, *11*, 237–243. [CrossRef] [PubMed]
17. Ripka, P.; Blažek, J.; Mirzaei, M.; Lipovský, P.; Šmelko, M.; Draganová, K. Inductive Position and Speed Sensors. *Sensors* **2019**, *20*, 65. [CrossRef] [PubMed]
18. Allers, M.; Reinecke, T.; Nagraik, T.; Solle, D.; Bakes, K.; Berger, M.; Scheper, T.; Zimmermann, S. Differential Inductive Sensor for Continuous Non-Invasive Cell Growth Monitoring in Disposable Bioreactors. *Proceedings* **2017**, *1*, 518. [CrossRef]
19. Karbeyaz, B.U.; Gençer, N.G. Electrical conductivity imaging via contactless measurements: An experimental study. *IEEE Trans. Med. Imaging* **2003**, *22*, 627–635. [CrossRef]
20. Tarjan, P.P.; McFee, R. Electrodeless Measurements of the Effective Resistivity of the Human Torso and Head by Magnetic Induction. *IEEE Trans. Biomed. Eng.* **1968**, *BME-15*, 266–278. [CrossRef] [PubMed]
21. Netz, J.; Forner, E.; Haagemann, S. Contactless impedance measurement by magnetic induction—A possible method for investigation of brain impedance. *Physiol. Meas.* **1993**, *14*, 463–471. [CrossRef]
22. Riedel, C.H. Planare induktive Impedanzmessverfahren in der Medizintechnik. Ph.D. Thesis, Universität Karlsruhe, Karlsruhe, Germany, 2004.

23. Zakaria, Z.; Rahim, R.A.; Mansor, M.S.B.; Yaacob, S.; Ayob, N.M.N.; Muji, S.Z.M.; Rahiman, M.H.F.; Aman, S.M.K.S. Advancements in transmitters and sensors for biological tissue imaging in magnetic induction tomography. *Sensors* **2012**, *12*, 7126–7156. [CrossRef]
24. Locatelli, F.; Di Filippo, S.; Manzoni, C. Relevance of the conductivity kinetic model in the control of sodium pool. *Kidney Int.* **2000**, *58*, S89–S95. [CrossRef]
25. Tura, A.; Sbrignadello, S.; Mambelli, E.; Ravazzani, P.; Santoro, A.; Pacini, G. Sodium concentration measurement during hemodialysis through ion-exchange resin and conductivity measure approach: In vitro experiments. *PLoS ONE* **2013**, *8*, e69227. [CrossRef] [PubMed]
26. Locatelli, F.; Buoncristiani, U.; Canaud, B.; Kohler, H.; Petitclerc, T.; Zucchelli, P. Haemodialysis with on-line monitoring equipment: Tools or toys? *Biosensors* **2005**, *20*, 22–33. [CrossRef]
27. Stragier, A.; Lopot, F.; Švára, F.; Polakovič, V. Fallacies and Pitfalls of Dialysis Sodium Prescription and Control. *Blood Purif.* **2018**, *46*, 27–33. [CrossRef] [PubMed]
28. Reynolds, R.M.; Padfield, P.L.; Seckl, J.R. Disorders of sodium balance. *BMJ* **2006**, *332*, 702–705. [CrossRef] [PubMed]
29. Locatelli, F.; La Milia, V.; Violo, L.; Del Vecchio, L.; Di Filippo, S. Optimizing haemodialysate composition. *Clin. Kidney J.* **2015**, *8*, 580–589. [CrossRef] [PubMed]
30. Stiller, S.; Bonnie-Schorn, E.; Grassmann, A.; Uhlenbusch-Körwer, I.; Mann, H. A Critical Review of Sodium Profiling for Hemodialysis. *Semin. Dial.* **2001**, *14*, 337–347. [CrossRef]
31. Ostermann, M.; Dickie, H.; Tovey, L.; Treacher, D. Management of sodium disorders during continuous haemofiltration. *Crit. Care* **2010**, *14*, 418. [CrossRef]
32. Darmon, M.; Pichon, M.; Schwebel, C.; Ruckly, S.; Adrie, C.; Haouache, H.; Azoulay, E.; Bouadma, L.; Clec'H, C.; Garrouste-Orgeas, M.; et al. Influence of early dysnatremia correction on survival of critically ill patients. *Shock* **2014**, *41*, 394–399. [CrossRef]
33. Palmer, B.F. Individualizing the Dialysate in the Hemodialysis Patient. *Semin. Dial.* **2001**, *14*, 41–49. [CrossRef] [PubMed]
34. De Paula, F.M.; Peixoto, A.J.; Pinto, L.V.; Dorigo, D.; Patricio, P.J.; Santos, S.F. Clinical consequences of an individualized dialysate sodium prescription in hemodialysis patients. *Kidney Int.* **2004**, *66*, 1232–1238. [CrossRef]
35. Paquette, F.; Goupil, R.; Madore, F.; Troyanov, S.; Bouchard, J. Continuous venovenous hemofiltration using customized replacement fluid for acute kidney injury with severe hypernatremia. *Clin. Kidney J.* **2016**, *9*, 540–542. [CrossRef]
36. Berger, M.; Sellering, F.; Rohrich, H.; Mansour, H.; Perl, T.; Zimmermann, S. A Differential Transformer for Noninvasive Continuous Sodium Monitoring During Dialysis Treatment. In Proceedings of the 2019 IEEE Sensors, Montreal, QC, Canada, 27–30 October 2019; pp. 1–4.
37. Berger, M.; Zygmanowski, A.; Sellering, F.; Röhrich, H.; Perl, T.; Mansour, H.; Zimmermann, S. Contactless and continuous sodium concentration monitoring during continuous renal replacement therapy. *Sens. Actuators B Chem.* **2020**, *320*, 128372. [CrossRef]
38. Pieralisi, M.; Di Mattia, V.; Petrini, V.; De Leo, A.; Manfredi, G.; Russo, P.; Scalise, L.; Cerri, G. An Electromagnetic Sensor for the Autonomous Running of Visually Impaired and Blind Athletes (Part I: The Fixed Infrastructure). *Sensors* **2017**, *17*, 364. [CrossRef] [PubMed]
39. Conway, J.T. Exact solutions for the mutual inductance of circular coils and elliptic coils. *IEEE Trans. Magn.* **2012**, *48*, 81–94. [CrossRef]
40. Massarini, A.; Kazimierczuk, M.K. Self-capacitance of inductors. *IEEE Trans. Power Electron.* **1997**, *12*, 671–676. [CrossRef]
41. Wu, Y.C.; Berezansky, P.A. Low Electrolytic Conductivity Standards. *J. Res. Natl. Inst. Stand. Technol.* **1995**, *100*, 521–527. [CrossRef] [PubMed]
42. Beving, H.; Eriksson, L.E.G.; Davey, C.L.; Kell, D.B. Dielectric properties of human blood and erythrocytes at radio frequencies (0.2–10 MHz): Dependence on cell volume fraction and medium composition. *Eur. Biophys. J.* **1994**, *23*, 207–215. [CrossRef]
43. Lehner, G. *Electromagnetic Field Theory for Engineers and Physicists*; Springer: Berlin/Heidelberg, Germany, 2008; ISBN 978-3-540-76305-5.
44. Kao, M.-S.; Chang, C.-F. *Understanding Electromagnetic Waves*; Springer International Publishing: Cham, Switzerland, 2020; ISBN 978-3-030-45707-5.
45. Davis, J.L. *Wave Propagation in Electromagnetic Media*; Springer: New York, NY, USA, 1990; ISBN 978-1-4612-7950-1.
46. MOOK, G.; Uchanin, V. Deep Penetrating Eddy Currents and Probes. *Mater. Test.* **2007**, *49*, 258–264. [CrossRef]
47. Assiry, A.M.; Gaily, M.H.; Alsamee, M.; Sarifudin, A. Electrical conductivity of seawater during ohmic heating. *Desalination* **2010**, *260*, 9–17. [CrossRef]
48. Dodd, C.V.; Deeds, W.E. Analytical Solutions to Eddy-Current Probe-Coil Problems. *J. Appl. Phys.* **1968**, *39*, 2829–2838. [CrossRef]
49. Mottl, Z. The quantitative relations between true and standard depth of penetration for air-cored probe coils in eddy current testing. *NDT Int.* **1990**, *23*, 11–18. [CrossRef]